Solid Freeform Fabrication 2021: Proceedings of the 32nd Annual International
Solid Freeform Fabrication Symposium – An Additive Manufacturing Conference
Reviewed Paper

AUTOMATED ANOMALY DETECTION OF LASER-BASED ADDITIVE MANUFACTURING USING MELT POOL SPARSE REPRESENTATION AND UNSUPERVISED LEARNING

Xiyue Zhao[1], Aidin Imandoust[2], Mojtaba Khanzadeh[3], Farhad Imani[1*], Linkan Bian[4]
[1]Department of Mechanical Engineering, University of Connecticut, Storrs, CT
[2]Department of Material Science and Engineering, University of North Texas, Denton, TX
[3]Amazon.com, Tempe, AZ
[4]Department of Industrial and Systems Engineering, Mississippi State University, Starkville, MS

*Corresponding author. Email: farhad.imani@uconn.edu

Abstract

Advanced thermal imaging is increasingly invested in direct energy deposition (DED) additive manufacturing (AM) to cope with information visibility of melt pool and tackle process inconsistency. However, there are key challenges regarding the feasibility of current image-guided monitoring methodologies in the DED process. First, high-resolution thermal images consist of millions of pixels captured by hundreds of frames lead to the curse of dimensionality in analysis. Second, the presence of various exogenous noise, ill-structured data, and significant cluster imbalance limit the capability of the current methodologies to perform real-time monitoring. The objective of this research is to advance the frontier of melt pool monitoring in DED process by designing an automated and unsupervised anomaly detection on high-dimensional thermal image data. Specifically, we develop a variational autoencoder to generate a low-dimensional representation of each input thermal image data. A Gaussian mixture model and K-Mean clustering are integrated with the generative model to split latent space into homogenous regions and detect anomalies. Experimental results show that the proposed methodology is highly effective in detecting defective melt pools with accuracy up to 94.52% and a false alarm rate of less than 2.1%.

Introduction

The ability of metallic additive manufacturing (AM) to produce intricate geometry parts (e.g., lattice structures and internal channels) from hard-to-process materials (e.g., Ti-6Al-4V and 17-4PH alloys) manifests their potential to revolutionize fabrication. This popularity is further driven by virtue of higher design flexibility, shorter development time, lower tooling cost, and less production waste. The manufacturing flexibility offered by AM is valuable in a variety of strategic applications ranging from aerospace to biomedical. For instance, using AM to make components for the Cessna Denali aircraft engine reduced the number of components from 855 to 12, and improved the fuel efficiency of the engine, as well as its power by over 10 percent [1]. However, the significant challenge of metal AM is the occurrence of various defects such as cracks, delamination, distortion, rough surface, lack of fusion, porosity, foreign inclusions, process instability (keyhole and balling), which in turn, deteriorate the builds strength, residual stress, hardness, and fatigue life [2-4]. As a result, the quality and reliability issues seen in many metals AM hamper further proliferation of this technology in mission-critical applications [5].

Porosity is the prominent type of defect in AM. The occurrence can be traced back to rapid solidification of AM parts, entrapped gas, incomplete powder melting, and lack of fusion [6]. The

thermal distribution of melt pool has received significant attention as a quality indicator since it provides underlying information about the complex physical and metallurgical processes, including heating, melting, Marangoni convection, evaporation, solidification, and morphology. In particular, the abnormal behavior of melt pool can be directly correlated to the formation of porosity, the most common type of defect in metallic AM.

Current defect detection methodologies are (1) offline (X-ray computed tomography (XCT) and ultra-sonic scanning) or (2) lumped-mass formulations, which are time-consuming, costly, and less effective with large-size builds [7]. Advancement in in-situ sensing technology provides an unprecedented opportunity for on-the-fly melt pool monitoring in various AM processes such as powder bed fusion (PBF) and direct energy deposition (DED). Significantly, the DED process offers the capability to produce and repair high-value and large-size components using Laser Engineered Net Shaping (LENS) and Direct Metal Deposition (DMD) systems. However, they suffer from a lack of part consistency and quality.

Images of the melt pool capture key thermal activities during the DED process, thus providing the most direct evidence of microstructural anomalies. For example, the small melt pool connecting to adjacent melt pools may cause porosity defects due to the presence of unmelted powder. Also, a large melt pool may develop remelting and overheating problems. The current image-guided monitoring focuses on analyzing the morphological features (e.g., length, depth, area, and size) or thermal distribution (average and maximum temperature) of melt pool. Therefore, the detection capability significantly relies on the quality of handcrafted features used in unsupervised learning models such as K-means [8], Gaussian mixture model (GMM) [9], and spectral clustering [10]. Recently, deep neural networks (DNNs) have shown remarkable ability in image-guided learning and autonomous feature extraction [11-13]. DNNs are less dependent on domain knowledge and simultaneously learn morphological features and thermal distribution through backpropagation by utilizing various building blocks (e.g., fully connected, convolutional, and pooling layers). However, there are fundamental challenges to the-state-of-the-art monitoring methods using thermal image streams:

1. ***High dimensionality and velocity:*** high-resolution images are comprised of thousands and millions of pixels. A standard video camera collects 24 frames per second, whereas a high-speed camera may acquire thousands of frames per second, which is a hurdle for real-time and image-guided monitoring.
2. ***Data structure:*** The low signal-to-noise ratio due to the DED by products (e.g., spatters, splashes, and fumes) significantly challenges the meaningful extraction of information. Furthermore, ill-structured data (e.g., different melt pools varying in sizes) and significant cluster imbalance (i.e., low number of defective images compared to the entire data) introduce uncertainty into the analysis. Hence, there is a dire need for robust methodologies that account for this uncertainty and realize real-time melt pool monitoring in DED.

The present research investigation is aimed at filling these gaps by developing an integrated deep generative model and unsupervised learning to automatically encode and discriminate meaningful patterns of variation in morphology and thermal distribution of images with significant cluster imbalance. Specifically, we design a variational autoencoder (VAE) model consists of an encoder (i.e., a recognition network) that converts the input to a latent representation and a decoder

(i.e., a generative network) that transforms the internal latent representation to the outputs. The VAE forms an information bottleneck, compresses high-dimensional image data into a low-dimensional latent space, and forces the encoder to extract the most critical features of defects into a continuous and meaningful embedding. Then, the GMM and K-mean clustering as unsupervised models are integrated with the variational information bottleneck to disentangle melt pool image data through useful discriminative features.

We evaluate and validate the proposed methodology with a real-world case study on thermal images captured from an OPTOMEC LENS 750 machine equipped with 1-kW Nd:YAG laser, pyrometer, and in-chamber thermal camera, which is used to build single track Ti-6A1-4V thin walls in Mississippi State University. Also, XCT of specimens are utilized to compare the predicted locations of pores based on the proposed methodology with their actual locations. The in-situ sensing and process monitoring and control are the next vertical steps to mitigate scrap and rework rates and further ensure the economic viability of AM. This project will eventually lead to the minimization of porosity during manufacturing as well as the maximization of final part strength and fatigue resistance.

The remainder of this paper is organized as follows: We first provide a literature review on the relevant methods of sensor-based flaw detection and melt pool characterization. Then the proposed deep generative model and unsupervised learning methodology are provided. Experimental design and materials along with experimental results on thin-wall structures are given in the next two sections. In the end, we conclude this paper by highlighting gaps in existing characterization methodologies for defect monitoring, then provide an overview of the proposed methodology.

Research Background

Sensor-based flaw detection:

Although empirical process mapping approaches have been utilized to avoid porosity, the occurrence of arbitrary defects is prevalent due to the dynamic condition of the DED process. Such random defects demand expensive and time-consuming post-build characterization. The XCT scanning and ultrasonic signal are among the most common offline sensing methods for defect characterization. The ultrasonic analysis is primarily investigated to quantify the mechanical strength and porous structure and find internal defects such as cracks, voids, delamination, to name a few [14]. However, it is sensitive to the selective layers of samples and ineffectual to capture pores between layers [15]. XCT has been extensively utilized not only to characterize the porosity level of build but also to link the variation in process parameters to the quality of final build [16, 17]. The limitations of the offline characterization methods are associated with cost and required time for analysis and the time restraint to leverage the unique layer-by-layer building mechanism of AM for in-process correction/control of defects before the next layer is built.

In-situ detection of defects using sensor signatures suggests the promise of reduced inspection cost and increased confidence in part quality. Five main types of signals are usually collected during the fabrication process; namely, visible lights and ultraviolet (UV) emitted from the plasma, IR emitted from the melt pool, ultrasonic waves from solid structure, audible sounds from air, and electric signals from plasma [18]. These signals can be captured with the photodiode, high-speed charge-coupled device (CCD) camera, complementary metal oxide semiconductor (CMOS) camera, and acoustic transducer [19, 20].

Acoustic signals are collected from the plasma that is generated at the powder bed surface. Using underheating or overheating of metal powder, the surface temperature of parts varies and causes a change in plasma density. Fluctuation of atmospheric pressure along with variation of plasma density impact the acoustic intensity and can be exploited as a process signature [21]. Although acoustic signals can also provide a high temporal resolution for tracking the location of defects more accurately, the background noise is noticeable for many AM processes, particularly for the laser metal AM processes that leverage inert gas in their chambers [22]. Optical-based techniques are the most widely adopted in-process monitoring methods in the DED community. Digital cameras, high-speed cameras, and infrared (IR) thermal cameras are commonly used to capture optical signals. In some cases, photodiodes and pyrometers can provide supplementary information [23]. Note that CCD or CMOS cameras fitted with near infrared (NIR) filters or infrared pyrometers are implemented to measure the shape, size, or temperature of the melt pool [24]. Photodiodes are integrated with the tube or nozzle to quantify the powder flow rates [25]. A camera is employed to ascertain the clad height in DED [26]. In addition, optical emission spectroscopy has been applied to monitor the optical emission above the melt pool that is created by a high-energy vapor plume [27].

Melt pool monitoring and characterization:

Melt pool images are the most informative process signatures for in-situ monitoring, as the shape and temperature of melt pools determine the occurrence of defects and dimensional accuracy. Therefore, various researchers have been designed statistical and machine learning methods to leverage sensing data from the melt pool for defect detection [28]. Khanzadeh et al. [29] investigated the effect of the heated zone on the emergence of flaws in DED. They demonstrated that by monitoring the features of melt pool images obtained from functional principal component analysis (FPCA) of dual-wavelength imaging pyrometer data, the onset of lack-of-fusion defects could be predicted through machine learning. Grasso et al. [30] integrated the plume images from an IR camera with a sampling frequency of 50 Hz and a spatial resolution of 320 × 240 pixels. The grayscale normalization was performed, and the regions of interest were extracted by image thresholding and segmentation. As such only the relevant portion of the image was used to effectively reduce computational cost and processing time of monitoring.

Supervised ML methods, including multilayer perceptron (MLP) and support vector machine (SVM), were applied to differentiate the distinctive thermal signatures of melt pools of overhang sections from bulk sections [31]. Kwon et al. [32] utilized the high-speed camera to simultaneously collect melt pool images and location information under different laser powers. DNNs were applied to accurately classify melt pool images concerning different laser powers, as it resulted in different levels of porosity. Although SVMs and DNNs may detect anomalies through melt pool images in DED, the lack of label in real-time sensing limit the ability of these supervised learning methods. To tackle this problem, K-means clustering was employed to detect and locate such defects in an unsupervised manner. The K-mean disentangled data since intensity profiles of melt pool images pixels of overheated regions significantly differ from the normal melting state [33]. Self-organizing map (SOM) is also applied to thermal profiles of melt pools to identify abnormal melt pools and predict porosity [5].

Although unsupervised learning is capable of differentiation of melt pool images based on the inherent structure in data, the lack of feature representation from ill-structured and noisy data limits

the capability to form a continuous and meaningful latent space. On the other hand, variational autoencoders have shown remarkable performance in unsupervised generative modeling of high-dimensional noisy data caused by complex distributions. VAEs as neural network-based models include two steps: encoding and decoding. The encoding step extracts nonlinear features automatically from original images to a low dimension matrix, which is called latent space. Then, extracted features could be converted to reconstructed images [34]. However, little has been done to leverage the sparse representation using VAEs for real-time defect detection in the DED process.

Research Methodology

This section presents the proposed methodology of sparse representation and unsupervised learning for defect monitoring using melt pool images in DED. As shown in Figure 1, our methodology is divided into the following steps: (1) melt pool image data acquisition, (2) synthetic data generation, (3) deep generative modeling, and (4) unsupervised learning of defects.

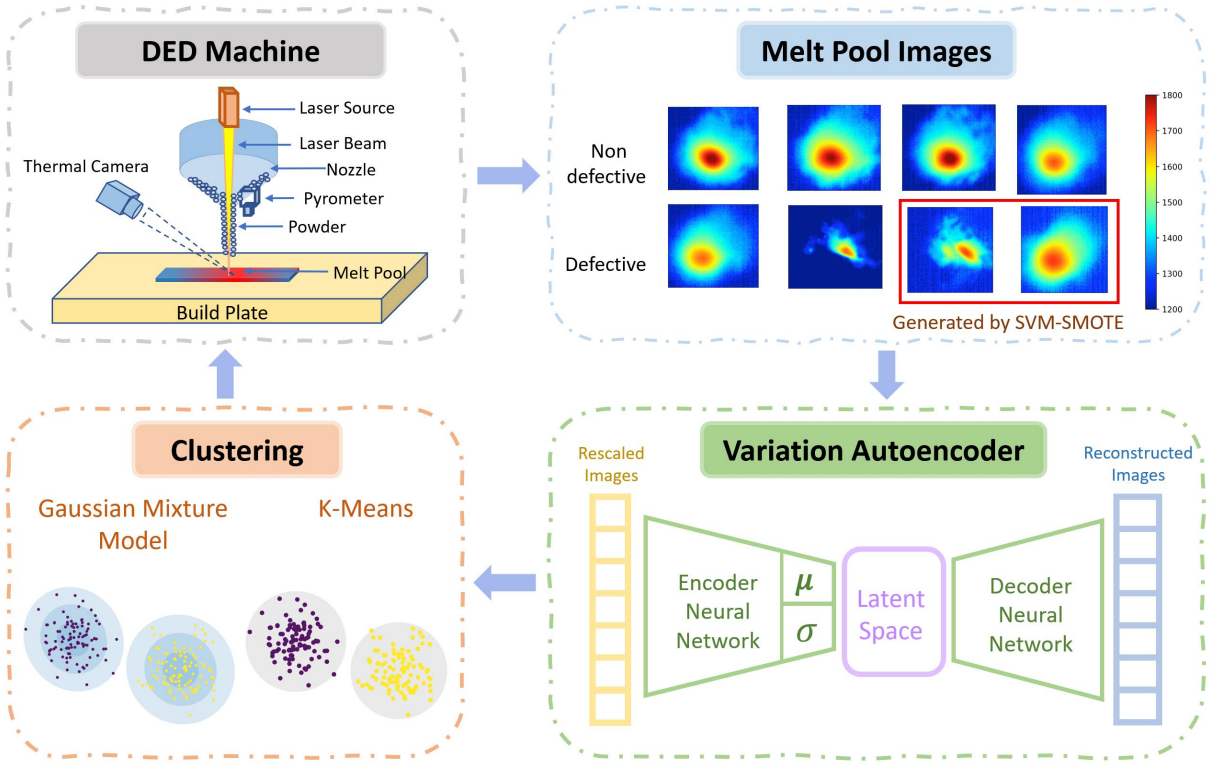

Figure 1. The flowchart of the proposed methodology for space representation and unsupervised learning of melt pool images in DED process.

Here, the VAE consists of an encoder (i.e., a recognition network) that converts the input to a latent representation and a decoder (i.e., a generative network) that transforms the internal latent representation to the outputs.

Part 1: Deep generative model for sparse representation:

The essence of VAE is to learn a stochastic mapping between the input space $\boldsymbol{x}$ with complex empirical distribution and latent space $\boldsymbol{z}$ with simpler distribution. The latent space $\boldsymbol{z}$ could be considered as a generated model with a joint distribution $p_{\boldsymbol{\theta}}(\boldsymbol{x}, \boldsymbol{z})$.

$$p_\theta(\boldsymbol{x},\boldsymbol{z}) = p_\theta(z)p_{\boldsymbol{\theta}}(\boldsymbol{x}|\boldsymbol{z}) \tag{1}$$

where $\boldsymbol{\theta}$ is a vector of the model's parameter, x and z represent each thermal image and the expression of $\boldsymbol{x}$ on latent space. The $p_{\boldsymbol{\theta}}(\boldsymbol{z})$ is a prior distribution over latent space and $p_{\boldsymbol{\theta}}(\boldsymbol{x}|\boldsymbol{z})$ is a stochastic decoder, a new distribution of $\boldsymbol{x}$ which is close to the original one conditioned on $\boldsymbol{z}$.

For VAE, the encoder and decoder are two neural networks and the likelihood function for training can be represented as Evidence Lower Bound (ELBO) [5]. The ELBO is the objective function of VAE and optimize the distribution q over latent space z as an approximation to the true posterior, $p_{\boldsymbol{\theta}}(\boldsymbol{z}|\boldsymbol{x})$. In the following equations $q_{\boldsymbol{\phi}}(\boldsymbol{z}|\boldsymbol{x})$ represents the stochastic encoder:

$$log p_{\boldsymbol{\theta}}(\boldsymbol{x}) = E_{q_{\boldsymbol{\phi}}(\boldsymbol{z}|\boldsymbol{x})}[log p_{\boldsymbol{\theta}}(\boldsymbol{x})] = \mathbb{E}_{q_{\boldsymbol{\phi}}(\boldsymbol{z}|\boldsymbol{x})}\left[\log\left[\frac{p_{\boldsymbol{\theta}}(\boldsymbol{x},\boldsymbol{z})}{p_{\boldsymbol{\theta}}(\boldsymbol{z}|\boldsymbol{x})}\right]\right] \tag{2}$$

$$= \mathbb{E}_{q_{\boldsymbol{\phi}}(\boldsymbol{z}|\boldsymbol{x})}\left[\log\left[\frac{q_{\boldsymbol{\phi}}(\boldsymbol{z}|x)}{p_{\boldsymbol{\theta}}(\boldsymbol{z}|\boldsymbol{x})}\right]\right] + \mathbb{E}_{q_{\boldsymbol{\phi}}(\boldsymbol{z}|\boldsymbol{x})}\left[\log\left[\frac{p_{\boldsymbol{\theta}}(x,z)}{q_{\boldsymbol{\phi}}(\boldsymbol{z}|\boldsymbol{x})}\right]\right] \tag{3}$$

The first part of Eq. (3) denotes Kullback-Leibler (KL) divergence between $q_{\boldsymbol{\phi}}(\boldsymbol{z}|\boldsymbol{x})$ and $p_{\boldsymbol{\theta}}(\boldsymbol{z}|\boldsymbol{x})$:

$$D_{KL}(q_{\boldsymbol{\phi}}(\boldsymbol{z}|\boldsymbol{x})||p_{\boldsymbol{\theta}}(\boldsymbol{z}|\boldsymbol{x})) = \mathbb{E}_{q_{\boldsymbol{\phi}}(\boldsymbol{z}|\boldsymbol{x})}[\log[p_{\boldsymbol{\theta}}(\boldsymbol{z}|\boldsymbol{x})]] - \mathbb{E}_{q_{\boldsymbol{\phi}}(\boldsymbol{z}|\boldsymbol{x})}\left[\log\left[q_{\boldsymbol{\phi}}(\boldsymbol{z}|\boldsymbol{x})\right]\right] \geq 0 \tag{4}$$

If and only if $q_{\boldsymbol{\phi}}(\boldsymbol{z}|\boldsymbol{x})$ equivalents to the true posterior distribution, the above Equation has a value of zero. The second part of Equation (3) denotes ELBO:

$$\mathcal{L}_{\boldsymbol{\theta},\boldsymbol{\phi}}(x) = \mathbb{E}_{q_{\boldsymbol{\phi}}(\boldsymbol{z}|\boldsymbol{x})}\left[\log\left[\frac{p_{\boldsymbol{\theta}}(\boldsymbol{x},\boldsymbol{z})}{q_{\boldsymbol{\phi}}(\boldsymbol{z}|x)}\right]\right] \tag{5}$$

$$= log p_{\boldsymbol{\theta}}(\boldsymbol{x}) - D_{KL}(q_{\boldsymbol{\phi}}(\boldsymbol{z}|\boldsymbol{x})||p_{\boldsymbol{\theta}}(\boldsymbol{z}|\boldsymbol{x})) \tag{6}$$

$$\leq log p_{\boldsymbol{\theta}}(\boldsymbol{x}) \tag{7}$$

KL-divergence shows the magnitude of distinction between two distributions. The less the KL-divergence is, the much similar the distributions of encoder and decoder are. The goal of VAE is to maximize $log p_{\boldsymbol{\theta}}(\boldsymbol{x})$ and to minimize the difference between $q_{\boldsymbol{\phi}}(\boldsymbol{z}|\boldsymbol{x})$ and $p_{\boldsymbol{\theta}}(\boldsymbol{z}|\boldsymbol{x})$. One of the most important properties of ELBO is that it allows us to use stochastic gradient descent (SGD) or Adam (i.e., an algorithm that combines properties of AdaGrad and RMSProp algorithms to handle sparse gradients on noisy problems) for joint optimization of encoder and decoder [35]. We random assign initial values of parameters ($\boldsymbol{\phi}$ and $\boldsymbol{\theta}$), and they will be stochastically optimized until convergence. To make the formulation tractable in VAE, we usually assume that $q_{\boldsymbol{\phi}}(\boldsymbol{z}|x)$ follows Gaussian distribution:

$$q_{\boldsymbol{\phi}}(\boldsymbol{z}|\boldsymbol{x}) = N(\boldsymbol{\mu},\boldsymbol{\sigma}^2) \tag{8}$$

where $\boldsymbol{\mu},\boldsymbol{\sigma}$ are mean and standard deviation of latent space obtained from the encoder. Setting $\boldsymbol{z} = \boldsymbol{\mu} + \boldsymbol{\sigma} \odot \boldsymbol{\epsilon}$, where $\boldsymbol{\epsilon}\sim N(0,\boldsymbol{I})$ and $\odot$ is the element-wise product. Then the ELBO's Monte Carlo estimator could be reduced to:

$$\mathcal{L}_{\boldsymbol{\theta},\boldsymbol{\phi}}(\boldsymbol{x}) = \mathbb{E}_{q_{\boldsymbol{\phi}}(\boldsymbol{z}|\boldsymbol{x})}\left[\log\left[\frac{p_{\boldsymbol{\theta}}(\boldsymbol{x},\boldsymbol{z})}{q_{\boldsymbol{\phi}}(\boldsymbol{z}|\boldsymbol{x})}\right]\right] \tag{9}$$

$$= \mathbb{E}_{q_{\boldsymbol{\phi}}(\boldsymbol{z}|\boldsymbol{x})}[log\ (p_{\boldsymbol{\theta}}(\boldsymbol{x}|\boldsymbol{z}))] - D_{KL}[q_{\boldsymbol{\phi}}(\boldsymbol{z}|\boldsymbol{x})||p_{\boldsymbol{\theta}}(\boldsymbol{z})] \tag{10}$$

$$= \frac{1}{N}\sum_{n}^{N} ln\big(p_{\boldsymbol{\theta}}(\boldsymbol{x}|\boldsymbol{z})\big) - \frac{1}{2}\sum_{l}^{L}(1 + ln(\sigma_l{}^2) - \sigma_l{}^2 - \mu_l{}^2) \tag{11}$$

where L is the dimension of latent space and N is the number of thermal images. There are no shared latent vectors among all data points for VAE, which means the ELBO loss of each data point is independent. Therefore, the ELBO objective is the sum of each data point's ELBO could be represented as Eq (8). For training VAE, we would like to minimize $\mathcal{L}_{\boldsymbol{\theta},\boldsymbol{\phi}}(\mathfrak{D})$.

$$\mathcal{L}_{\boldsymbol{\theta},\boldsymbol{\phi}}(\mathfrak{D}) = \sum_{\boldsymbol{x}\in\mathcal{D}} \mathcal{L}_{\boldsymbol{\theta},\boldsymbol{\phi}}(\boldsymbol{x}) \tag{12}$$

We design our neural networks in a way that both encoder and decoder contain 4 layers. The constructions of these two neural networks are set to be different. The architecture of encoder and decoder neural networks are represented in Figure 2. A rectified linear activation function (ReLu) is applied for activation functions of all hidden layers. Our model is optimized by Adam optimizer to obtain a better weight for the neural network using noisy manufacturing images.

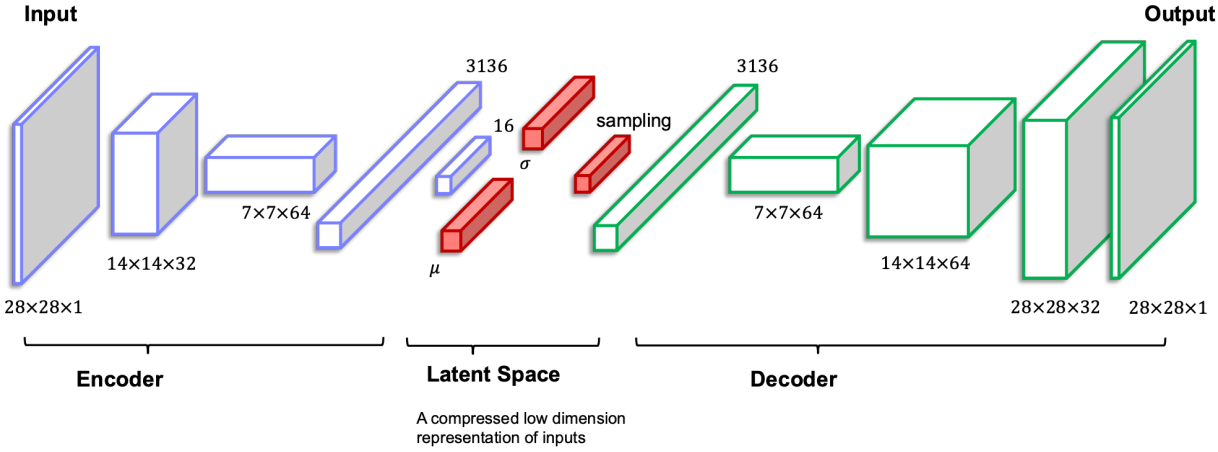

Figure 2. Neural networks architecture of variational autoencoder for thermal images.

Part 2: Synthetic minority over-sampling technique

The unbalanced data in AM setting (i.e., low number of images representing defective regions compared to the whole number of images) prevents the VAE model from learning the decision boundary effectively. Synthetic Minority Over-sampling Technique (SMOTE), as one of the common methods, could generate minority cluster data to make the dataset balanced by oversampling the original dataset [36]. Therefore, we leverage SVM-SMOTE to generate some abnormal melt pool images. For SVM-SMOTE, the borderline area is identical to the support vectors, which are achieved by training traditional Support Vector Machine (SVM) on the original datasets [33]. New data could be created by order of the first nearest neighbor to the k^{th} nearest neighbor instead of choosing the neighbors randomly. In general, minority cluster (i.e., a group of images portraying defective region in a build) is considered as positive and majority cluster (i.e., non-defective) is treated as negative. SVM-SMOTE trains the SVM on the inputs firstly to get the set of positive support vectors $\boldsymbol{SV}^+$ and distribute input among them evenly. Combine k positive nearest neighbors of each $\boldsymbol{SV}^+$ to get an array as $\boldsymbol{nn}$. After that, if half of m nearest neighbors

come from negative cluster, $AA = \{aa_t\}_{t=1}^{T}$, where T is the number of positive support vectors, then is considered as an array contains the number of generated data corresponding to each positive SV. Next, we create aa_i new positive class data among the lines joining $\boldsymbol{sv}_i^+$ with its k positive nearest neighbors. The generated melt pool images can be represented as

$$\boldsymbol{x}_{new}^+ = \boldsymbol{sv}_i^+ + \rho \times (\boldsymbol{sv}_i^+ - \boldsymbol{nn}_{i,j}) \tag{13}$$

where $\rho \in [0,1]$ and $\boldsymbol{nn}_{i,j}$ is the j^{th} minority nearest neighbor of $\boldsymbol{sv}_i^+$. On the contrary, the generated data can be expressed by

$$\boldsymbol{x}_{new}^+ = \boldsymbol{sv}_i^+ + \rho \times (\boldsymbol{nn}_{i,j} - \boldsymbol{sv}_i^+) \tag{14}$$

Finally, we could get balanced data by combining the original data and generated data.

Part 3: T-distributed stochastic neighbor embedding dimension reduction

T-distributed stochastic neighbor embedding (t-SNE) is one of the statistical models which maps high-dimensional data to two or three dimensions for each data point [37]. It is a nonlinear dimensionality reduction algorithm, which is suitable for visualizing high-dimensional data by embedding it into lower dimensions. t-SNE converts the distance between the data points in the original space into a Gaussian distribution probability. The closer the distance in high-dimensional space is, the larger the probability. In our case, for vitalizing location of images after mapping them into latent space more clearly. t-SNE is used for reducing the dimension of latent variables from N to 2. It computes the proportional to the similarity of objects x_i, x_j:

$$p_{j|i} = \frac{\exp\left(-d(\boldsymbol{z}_i, \boldsymbol{z}_j)/2\sigma_i^2\right)}{\sum_{k \neq i} \exp\left(-d(\boldsymbol{z}_i, \boldsymbol{z}_j)/2\sigma_i^2\right)}, p_{i|i} = 0 \tag{15}$$

where $\boldsymbol{z}_i$ is the latent variables of a melt pool image, $i, j \in L$, and $i \neq j$. After mapping $\boldsymbol{z}_i$ into 2D, we could get y_i, which corresponds to z_i. Eq. (16) leverages Student-t Distribution to represent the similarity of y_i, y_j:

$$q_{ij} = \frac{(1 + ||y_i - y_j||^2)^{-1}}{\sum_{k \neq l}(1 + ||y_k - y_l||^2)^{-1}}, q_{i|i} = 0 \tag{16}$$

where $i \neq j$. Then the location of y_i is determined by optimizing the KL divergence and the loss function as following:

$$KL(P|Q) = \sum_{i \neq j} p_{ij} log \frac{p_{ij}}{q_{ij}} \tag{17}$$

A gradient descent algorithm is used for minimizing KL divergence. Here, y_i is corresponding to the result of minimization.

Part 4: Clustering models

In this part, we are using two different methods to do the clustering: Gaussian Mixture Model (GMM) and K-Means. We are interested in finding out whether the latent variables of VAE explain their cluster. Therefore, the constructed latent values are the inputs of these two clustering methods. Both for K-Means and GMM are trained with an assumption that the number of clustering is 2.

K-Means:

K-Means is an iterative clustering algorithm based on squared Euclidean distance. This method aims to assign N observations into k clusters in which every observation belongs to a cluster with

the closest squared Euclidean distance. Here, $k = 2$. In our study, we use standard K-Means to do the clustering, and the algorithm proceeds as follows:

1. Choose a set of *k* means as initial cluster centroids $\boldsymbol{m} = \boldsymbol{m}_1, \boldsymbol{m}_2, \dots, \boldsymbol{m}_k$.
2. For each latent space point, calculate Euclidean distance to every centroid and assign each observation according to the Voronoi diagram generated by the means.

$$\boldsymbol{S}_i^{(t)} = \{\boldsymbol{z}_p : \left\|\boldsymbol{z}_p - \boldsymbol{m}_i^{(t)}\right\| \leq \left\|\boldsymbol{z}_p - \boldsymbol{m}_j^{(t)}\right\|^2 \forall j, 1 \leq j \leq k\} \tag{18}$$

3. Recalculate the centroids of each cluster.

$$\boldsymbol{m}_j^{(t+1)} = \frac{1}{\boldsymbol{S}_i^{(t)}} \sum_{\boldsymbol{z}_j \in \boldsymbol{S}_i^{(t)}} \boldsymbol{z}_j \tag{19}$$

4. Repeat steps 2 and 3 until the convergence.

Gaussian mixture model:

GMM is an extension of a single Gaussian probability density function. The model is comprised of several different single Gaussians. Each Gaussian is regarded as a cluster according to the different parameters of the normal probability density function (PDF). By computing the PDF of the input, the typical cluster of the input could be determined by a threshold. The PDF of inputs could be represented as Eq. (20):

$$P(\boldsymbol{z}_i) = \sum_{j=1}^{M} a_j N_j(\boldsymbol{z}_i; \boldsymbol{\mu}_j, \boldsymbol{\Sigma}_j) \tag{20}$$

where x_i is the latent variables of an image in our case and $\sum_{k=1}^{K} a_k = 1$. a_j is the weight factor and denotes the probability of choosing the k^{th} Gaussian model. With the sample points with unknown specified classification, the model parameters $(a, \boldsymbol{\mu}, \boldsymbol{\Sigma})$ could be calculated. The likelihood function of $\{\boldsymbol{z}_1, \dots, \boldsymbol{z}_N\}$ is:

$$L(a, \boldsymbol{\mu}, \boldsymbol{\Sigma}) = L(\boldsymbol{z}_1, \dots, \boldsymbol{z}_N; a, \boldsymbol{\mu}, \boldsymbol{\Sigma}) = \prod_{n=1}^{N} p(\boldsymbol{z}_n; a, \boldsymbol{\mu}, \boldsymbol{\Sigma}) = \prod_{n=1}^{N} \sum_{k=1}^{K} a_k N(\boldsymbol{z}_n; \boldsymbol{\mu}_k, \boldsymbol{\Sigma}_k) \tag{21}$$

Finally, we set the derivation of $lnL(a, \boldsymbol{\mu}, \boldsymbol{\Sigma})$ to zero and obtain optimal $(a, \boldsymbol{\mu}, \boldsymbol{\Sigma})$.

Experimental Design and Materials

This section presents equipment for acquiring melt pool images in this real-world case study. An OPTOMEC Lens 750 machine equipped with a 1-kW Nd: YAG laser, pyrometer, and an in-chamber thermal camera (Figure 3(a)) are utilized to fabricate single-track Ti-6AI-4V thin walls (Figure 3(b)). The experiment was performed at Mississippi State University with popular Lens technique in DED process that has the capability to create functionally graded materials [5]. To predict the porosity occurrence and the time-varying evolution of melt pool dynamics, a built-in thermal imaging system is integrated. Temperature distribution of the top surface of melt pool during fabrication is recorded by a dual-wavelength pyrometer (Stratonics, Inc.). Due to the specified exposure time (2.0274 ms) for a given collection rate of the pyrometer, the sensor could reduce the chance of blur resulting from motion compared to the IR camera. In this experiment, the laser's scan rate and build move are set to 12.7 mm/s and 26 μm in each exposure time. There is a CMOS detector applied in the pyrometer with 752×480 pixels and 6.45 μm for each pixel

size. The temperature in the pyrometer has a range of 1000 to 2500℃. The exposure time and pixel clock to 2.0274 ms and 5 MHz, respectively.

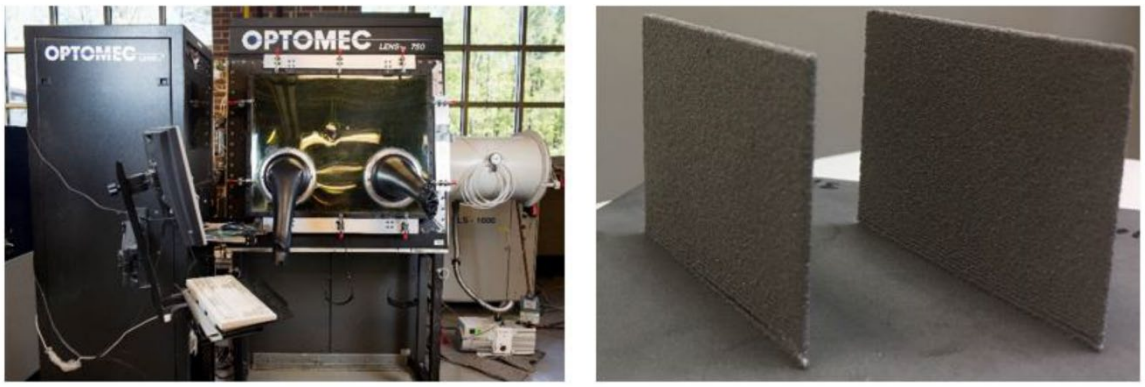

(a) (b)

Figure 3. (a) The advanced imaging system installed in the OPTOMEC LENS 750 machine, and (b) final thin wall builds using Ti-6Al-4V material [5].

Because of the high image resolution (1.7 MB for each melt pool image) and monitoring frequency, the build of a single thin wall (length = 47.81 mm, height = 27.56 mm, thickness = 1.78 mm) brings about 4.7 GB of image stream data.

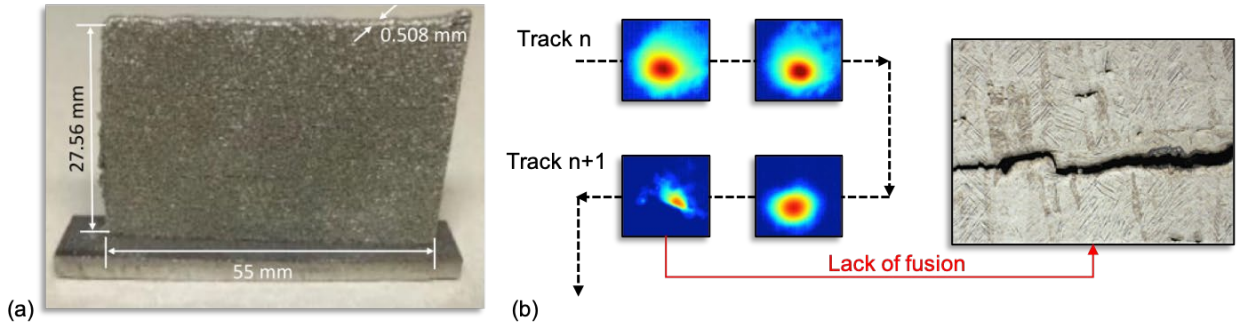

Figure 4. (a) The image of the thin wall, and (b) The relationship between meltpool characteristics and lack of fusion.

Figure 4 demonstrates the potential relationship between characteristics of melt pool images and lack of fusion from our experimental data. Note that the color of meltpool indicates the temprature of the melp pool. After obtaining the data, a radon transform is applied to reconstruct the image using the acquired X-ray intensity readings for each of the detector elements. Then the individual slice images could be accumulated into a 3D reconstruction. Next, a 3D reconstruction could be generated by accumulation of the individual slice images. The porosity of the as-built part, which is derived from melt pool characteristics, is compared with the XCT characterization. The thermal image data are processed and stored in1564 thermal image files, each of which contains 480×752 cells of information. The area of the melt pool is extracted based on the melt pool temperature of Ti-6Al-4V(T_γ=1636˚C). Each melt pool is scaled using the coordinates of the peak temperature. The accuracy of prediction is examined by finding the proportion of pores, which are predicted correctly using the melt pool clustering method, in total pores.

Experimental Results

In this section, we perform the experimental study on our dataset with the proposed methodology. To prevent overfitting, we perform K-fold cross validation with different fold numbers. Note that we have 1493 positive instances (i.e., defective images) and 71 (i.e., non-defective images) negative instances in our data. We first performed SMOTE-SVM to balance the positive and negative cases for VAE construction; therefore, we have in total 2896 instances. We trained the VAE based on the proposed methodology and run each experiment 20 times. Note that each image has a size of 28 × 28. We investigate VAE-Kmeans and VAE-GMM with different dimensions of latent space (L=2, 5, 10, 100, 1000) and the number of folds (K = 2, 3, 4, 5).

We first utilize the t-SNE to visualize the embedded latent space of the whole dataset. As shown in Figure 4, the trend of separation can be seen from a) to e). Each node in the t-SNE visualization is corresponding to one image in the dataset.

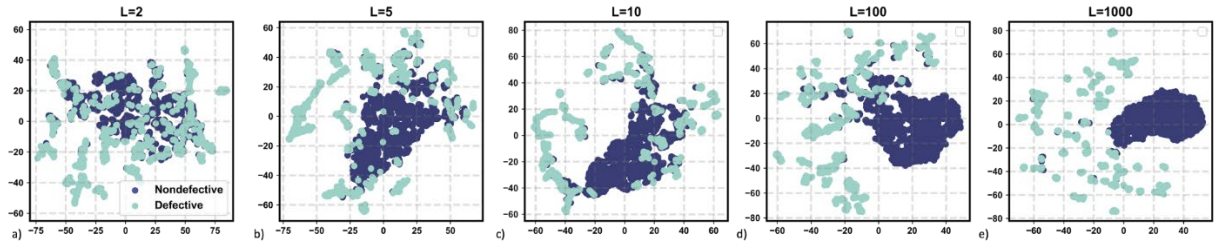

Figure 4. t-SNE embedding of the latent space based on the number of latent in VAE, a) number of latent L=2, b) number of latent L=5, and c) number of latent L=10, d) number of latent L=100, and e) number of latent L=1000.

Figure 4 a) shows the nodes from two classes are overlapped with each other, indicating that the two-dimensional latent space embedding cannot extract enough useful information to express the distinction of two classes. However, with the increment of the number of latent L, the distinction between two groups can be clearly visualized through t-SNE embedding. In Figure 4 (e), only a few images are misclassified into the other group.

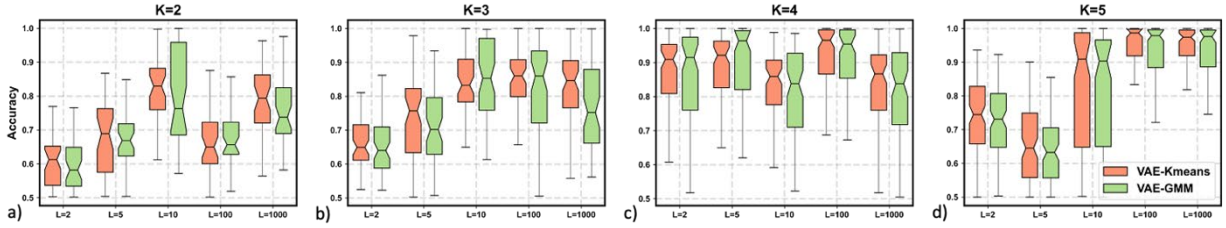

Figure 5. The accuracy of porosity detection using the proposed VAE-KMeans and VAE-GMM when embedding to different number of latent for a) 2 folds, b) 3 folds, c) 4 folds, and d) 5 folds.

Figure 5 illustrates the accuracy of porosity detection using the proposed VAE-KMeans and VAE-GMM when embedding to different numbers of latent for a) 2 folds, b) 3 folds, c) 4 folds, and d) 5 folds. As shown in Figure 5, the overall trend of detection accuracy increases when the number of latent increases. However, the number of latent that brings the best detection accuracy under different fold numbers varies. For example, the best choice for the number of latent L=10 while K=2, and L=100 is a better option when K=2 since under different values of K, the number

of training data and testing data are different. The training set has more data when K=2 in comparison with K=3. It can be seen that less amount of training data needs more dimensions in latent to have a better detection accuracy. Also, it is worth mentioning that the accuracies under L=1000 among the four subplots in Figure 5 are not the highest, indicating that a higher dimension in latent space does not necessarily mean that it can capture all the hidden information from melt pool images and provide a better detection result. Instead, it might pick redundant features from the images. As shown in Figure 5 (c) and Figure 5 (d), the accuracies under different L could reach 0.9. Even though the accuracies when $L = 100$ are the highest among all experiments when $K = 5$, all accuracies under different L are higher than 0.7 when $K = 4$, which means it performs better than $K = 5$ and the computational cost is lower. Overall, K=4 results in a better porosity detection accuracy with the consideration of the computational complexity. Further, we construct the confusion matrix and report the sensitivity (*SEN*), specificity (SPC), precision (PPV), and F-scores, respectively, under $K = 4$. The results of the experiment are provided in Table 1.

Table 1. Sensitivity (SEN), specificity (SPC), precision (PPV), and F-scores of porosity detection using the proposed VAE-KMeans and VAE-GMM model when K=4.

Number of Latent	Sensitivity (SEN)		Specificity (SPC)		Precision (PPV)		F-score	
	K-Means	GMM	K-Means	GMM	K-Means	GMM	K-Means	GMM
L=2	81.43%	75.54%	93.85%	93.11%	92.13%	89.47%	85.13%	79.62%
L=5	81.53%	84.63%	94.86%	95.26%	92.33%	93.06%	85.31%	86.98%
L=10	76.00%	74.97%	89.37%	87.91%	86.60%	85.71%	79.63%	77.42%
L=100	86.06%	85.59%	94.12%	93.86%	93.07%	93.09%	88.55%	87.05%
L=1000	72.87%	71.59%	91.70%	91.30%	88.53%	89.26%	78.64%	75.87%

Sensitivity, Recall, Precision, F-score, which account for the accuracy, are represented by the following equations,

$$Sensitivity\ (SEN) = \frac{TP}{TP + FN} \tag{22}$$

$$Specificity\ (SPC) = \frac{TN}{TN + FP} \tag{23}$$

$$Precision\ (PPV) = \frac{TP}{TP + FP} \tag{24}$$

$$F - score = \frac{2 \times (PPR \times TPR)}{PPV + TPR} \tag{25}$$

where TP, FN, FP, TN are representing true positive, false negative, false positive, and true negative in the confusion matrix, respectively. Interestingly, when $L = 100$, the values of F-scores are highest both for K-Means and GMM, resulting in 0.885±0.0156 and 0.871±0.0172, which indicates the highest accuracies in terms of porosity prediction.

Conclusion

In-situ thermal image sensing systems are recently developed to address the quality challenge in DED. However, they are still at an early age and are limited in the ability to analyze generated data in real-time. The presence of high-dimensional, low signal-to-noise ratio, and ill-structured data without annotation hinders real-time defect detection in the process. There is an urgent need to integrate real-time thermal image data with newly developed machine learning methods and realize the qualify-as-you-build paradigm in DED. We validate the proposed porosity prediction

method by benchmarking against the X-ray CT characterization of a Ti-6Al-4V thin wall build fabricated using a LENS system. The comparative study with a previous work that focuses on the morphological features of melt pools (e.g., area, length, width, etc.) shows significant improvement in prediction accuracy. The clustering based on morphological features fails to form distinct clusters, which indicates that simple features are not sufficient for the identification of anomalies. The structure of melt pool images can be learned through the sparse representation model that encodes both morphological features and thermal distribution automatically.

Acknowledgment

The authors gratefully acknowledge the valuable contributions from the Center for Advanced Vehicular Systems (CAVS) at Mississippi State University for this research.

Reference

[1] A. Gaikwad, R. Yavari, M. Montazeri, K. Cole, L. Bian and P. Rao, "Toward the digital twin of additive manufacturing: Integrating thermal simulations, sensing, and analytics to detect process faults," *IISE Transactions,* vol. 52, *(11),* pp. 1204-1217, 2020.

[2] F. Imani, A. Gaikwad, M. Montazeri, P. Rao, H. Yang and E. Reutzel, "Process mapping and in-process monitoring of porosity in laser powder bed fusion using layerwise optical imaging," *Journal of Manufacturing Science and Engineering,* vol. 140, *(10),* 2018.

[3] B. Torries, A. Imandoust, S. Beretta, S. Shao and N. Shamsaei, "Overview on microstructure-and defect-sensitive fatigue modeling of additively manufactured materials," *Jom,* vol. 70, *(9),* pp. 1853-1862, 2018.

[4] B. Torries, R. Shrestha, A. Imandoust and N. Shamsaei, "Fatigue Life Prediction of Additively Manufactured Metallic Materials Using a Fracture Mechanics Approach," *Solid Freeform Fabrication,* pp. 11811190, 2018.

[5] M. Khanzadeh, S. Chowdhury, M. A. Tschopp, H. R. Doude, M. Marufuzzaman and L. Bian, "In-situ monitoring of melt pool images for porosity prediction in directed energy deposition processes," *IISE Transactions,* vol. 51, *(5),* pp. 437-455, 2019.

[6] F. Imani, A. Gaikwad, M. Montazeri, P. Rao, H. Yang and E. Reutzel, "Layerwise in-process quality monitoring in laser powder bed fusion," in *ASME 2018 13th International Manufacturing Science and Engineering Conference,* 2018, p. V001T01A038.

[7] M. Khanzadeh, P. Rao, R. Jafari-Marandi, B. K. Smith, M. A. Tschopp and L. Bian, "Quantifying geometric accuracy with unsupervised machine learning: Using self-organizing map on fused filament fabrication additive manufacturing parts," *Journal of Manufacturing Science and Engineering,* vol. 140, *(3),* 2018.

[8] A. Bansal, M. Sharma and S. Goel, "Improved K-mean clustering algorithm for prediction analysis using classification technique in data mining," *International Journal of Computer Applications,* vol. 157, *(6),* pp. 975, 2017.

[9] J. J. Verbeek, N. Vlassis and B. Kröse, "Efficient greedy learning of Gaussian mixture models," *Neural Comput.,* vol. 15, *(2),* pp. 469-485, 2003.

[10] J. Liu and J. Han, "Spectral clustering," in *Data Clustering*Anonymous Chapman and Hall/CRC, 2018, pp. 177-200.

[11] F. Imani, R. Chen, E. Diewald, E. Reutzel and H. Yang, "Deep learning of variant geometry in layerwise imaging profiles for additive manufacturing quality control," *Journal of Manufacturing Science and Engineering,* vol. 141, *(11),* 2019.
[12] A. Gaikwad, F. Imani, H. Yang, E. Reutzel and P. Rao, "In Situ Monitoring of Thin-Wall Build Quality in Laser Powder Bed Fusion Using Deep Learning," *Smart and Sustainable Manufacturing Systems,* vol. 3, *(1),* 2019.
[13] A. Mirzaei, A. Zarei-Hanzaki, M. H. Pishbin, A. Imandoust and S. Khoddam, "Evaluating the hot deformation behavior of a super-austenitic steel through microstructural and neural network analysis," *Journal of Materials Engineering and Performance,* vol. 24, *(6),* pp. 2412-2421, 2015.
[14] A. Chabot, N. Laroche, E. Carcreff, M. Rauch and J. Hascoët, "Towards defect monitoring for metallic additive manufacturing components using phased array ultrasonic testing," *J. Intell. Manuf.,* pp. 1-11, 2019.
[15] A. B. Lopez, J. Santos, J. P. Sousa, T. G. Santos and L. Quintino, "Phased array ultrasonic inspection of metal additive manufacturing parts," *J. Nondestr. Eval.,* vol. 38, *(3),* pp. 1-11, 2019.
[16] R. M. Yazdi, F. Imani and H. Yang, "A hybrid deep learning model of process-build interactions in additive manufacturing," *J. Manuf. Syst.,* vol. 57, pp. 460-468, 2020.
[17] F. Imani, B. Yao, R. Chen, P. Rao and H. Yang, "Joint multifractal and lacunarity analysis of image profiles for manufacturing quality control," *Journal of Manufacturing Science and Engineering,* vol. 141, *(4),* 2019.
[18] J. P. Kruth, M. Bartscher, S. Carmignato, R. Schmitt, L. De Chiffre and A. Weckenmann, "Computed tomography for dimensional metrology," *CIRP Annals,* vol. 60, *(2),* pp. 821-842, 2011.
[19] B. M. Colosimo and M. Grasso, "On-Machine Measurement, Monitoring and Control," *Precision Metal Additive Manufacturing,* pp. 102, 2020.
[20] Q. Tian, S. Guo, E. Melder, L. Bian and W. Guo, "Deep Learning-Based Data Fusion Method for In Situ Porosity Detection in Laser-Based Additive Manufacturing," *Journal of Manufacturing Science and Engineering,* vol. 143, *(4),* p. 041011, 2021.
[21] S. A. Shevchik, C. Kenel, C. Leinenbach and K. Wasmer, "Acoustic emission for in situ quality monitoring in additive manufacturing using spectral convolutional neural networks," *Additive Manufacturing,* vol. 21, pp. 598-604, 2018.
[22] H. Wu, Z. Yu and Y. Wang, "A new approach for online monitoring of additive manufacturing based on acoustic emission," in *ASME 2016 11th International Manufacturing Science and Engineering Conference,* 2016, p. V003T08A013.
[23] J. C. Heigel, P. Michaleris and E. W. Reutzel, "Thermo-mechanical model development and validation of directed energy deposition additive manufacturing of Ti–6Al–4V," *Additive Manufacturing,* vol. 5, pp. 9-19, 2015.
[24] L. Song, V. Bagavath-Singh, B. Dutta and J. Mazumder, "Control of melt pool temperature and deposition height during direct metal deposition process," *The International Journal of Advanced Manufacturing Technology,* vol. 58, *(1),* pp. 247-256, 2012.
[25] D. A. Kriczky, J. Irwin, E. W. Reutzel, P. Michaleris, A. R. Nassar and J. Craig, "3D spatial reconstruction of thermal characteristics in directed energy deposition through optical thermal imaging," *J. Mater. Process. Technol.,* vol. 221, pp. 172-186, 2015.

[26] J. P. Davim, C. Oliveira and A. Cardoso, "Predicting the geometric form of clad in laser cladding by powder using multiple regression analysis (MRA)," *Mater Des,* vol. 29, *(2),* pp. 554-557, 2008.
[27] A. R. Nassar, T. J. Spurgeon and E. W. Reutzel, "Sensing defects during directed-energy additive manufacturing of metal parts using optical emissions spectroscopy," in *Solid Freeform Fabrication Symposium Proceedings,* 2014, pp. 278-287.
[28] C. Wang, X. P. Tan, S. B. Tor and C. S. Lim, "Machine learning in additive manufacturing: State-of-the-art and perspectives," *Additive Manufacturing,* pp. 101538, 2020.
[29] M. Khanzadeh, W. Tian, A. Yadollahi, H. R. Doude, M. A. Tschopp and L. Bian, "Dual process monitoring of metal-based additive manufacturing using tensor decomposition of thermal image streams," *Additive Manufacturing,* vol. 23, pp. 443-456, 2018.
[30] M. Grasso, A. G. Demir, B. Previtali and B. M. Colosimo, "In situ monitoring of selective laser melting of zinc powder via infrared imaging of the process plume," *Robot. Comput. Integrated Manuf.,* vol. 49, pp. 229-239, 2018.
[31] M. Montazeri and P. Rao, "Sensor-based build condition monitoring in laser powder bed fusion additive manufacturing process using a spectral graph theoretic approach," *Journal of Manufacturing Science and Engineering,* vol. 140, *(9),* 2018.
[32] O. Kwon, H. G. Kim, M. J. Ham, W. Kim, G. Kim, J. Cho, N. I. Kim and K. Kim, "A deep neural network for classification of melt-pool images in metal additive manufacturing," *J. Intell. Manuf.,* vol. 31, *(2),* pp. 375-386, 2020.
[33] M. Grasso, V. Laguzza, Q. Semeraro and B. M. Colosimo, "In-process monitoring of selective laser melting: spatial detection of defects via image data analysis," *Journal of Manufacturing Science and Engineering,* vol. 139, *(5),* 2017.
[34] L. Wang, Y. Chan, F. Ahmed, Z. Liu, P. Zhu and W. Chen, "Deep generative modeling for mechanistic-based learning and design of metamaterial systems," *Comput. Methods Appl. Mech. Eng.,* vol. 372, pp. 113377, 2020.
[35] D. P. Kingma and J. Ba, "ADAM: A method for stochastic optimization, ICLR2015," *arXiv Preprint arXiv:1412.6980,* vol. 9, 2015.
[36] N. V. Chawla, K. W. Bowyer, L. O. Hall and W. P. Kegelmeyer, "SMOTE: synthetic minority over-sampling technique," *Journal of Artificial Intelligence Research,* vol. 16, pp. 321-357, 2002.
[37] L. Van der Maaten and G. Hinton, "Visualizing data using t-SNE." *Journal of Machine Learning Research,* vol. 9, *(11),* 2008.
[38] M. Lan, Y. Zhang, L. Zhang and B. Du, "Defect detection from UAV images based on region-based CNNs," in *2018 IEEE International Conference on Data Mining Workshops (ICDMW),* 2018, pp. 385-390.